

**1 Large-Scale Clustering of Tropical Precipitation and its
2 Implications for the Radiation Budget across
3 Timescales**

4 P. Blackberg^{1,2}, Martin S. Singh^{1,2}

5 ¹School of Earth, Atmosphere, and Environment, Monash University, Victoria, Australia

6 ²Centre of Excellence for the Weather of the 21st Century, Monash University, Victoria, Australia

7 **Key Points:**

- 8 • Climate models project future increases in large-scale clustering of tropical pre-
9 cipitation and a meridional contraction of heavy rainfall
10 • Changes in clustering are sensitive to the Pacific SST gradient in observed and
11 simulated interannual variability and in model projections
12 • Effect of changes in clustering on the radiation budget depends on timescale, pre-
13 cluding an observational constraint on climate sensitivity

Abstract

The spatial organization of deep convection in tropical regions is posited to play an important role in determining characteristics of the tropical climate such as the humidity distribution and cloudiness and may therefore be an important control on climate feedbacks. This study analyzes one aspect of convective organization, the clustering of heavy precipitation on large scales, in both interannual variability and under warming in future climate projections. Both observations and global climate models indicate that large-scale clustering is sensitive to the SST gradient in the Pacific, being largest during El Niño events. Under future warming, models project an increase in clustering with a large intermodel spread. The increase is associated with a narrowing of the intertropical convergence zone, while the model spread is partially explained by differences in projections of the SST gradient in the Pacific. Both observations and models indicate large-scale clustering influences the cloud and humidity distributions, albeit with some differences. However, the intermodel spread in changes in clustering with warming is not related to the intermodel spread in projections of tropical-mean relative humidity or low cloudiness in regions of descent, precluding attempts to provide an observational constraint on feedbacks or climate sensitivity. Nevertheless, the tendency for a meridional contraction of precipitation explains about 45% of the variance in projected drying, highlighting the narrowing of the ITCZ as an important aspect of large-scale convective organization in a warmer climate.

Plain Language Summary

The spatial distribution of rainfall in the tropics is expected to change in a warming climate, with potentially important impacts on how much radiation is absorbed by water vapor and reflected by clouds. This study shows that heavy rainfall tends to move towards the equator and to the Pacific Ocean in projections with global climate models, resulting in an overall increase in the "clustering" of rainfall on the large scale. Further, the results show a shift in rainfall to the equator with global warming is associated with a drying of the tropical atmosphere, which may have an influence on how much the planet warms for a given CO_2 change. However, similar observed shifts in rainfall in the current climate are not found to have the same effect on humidity and clouds as for changes with warming, suggesting caution should be exercised when using relationships derived from observations to predict future changes.

46 **1 Introduction**

47 The spatial organization of deep convection in tropical regions plays a critical role
 48 in shaping the hydrological cycle and the moisture and cloud distribution (Hartmann
 49 et al., 1984). Changes in organization with warming may therefore have implications for
 50 a range of climatic processes, including precipitation extremes (e.g., Pendergrass et al.,
 51 2016; Bao et al., 2017; Semie & Bony, 2020) and the radiative feedbacks that control equi-
 52 librium climate sensitivity (ECS) (e.g., Emanuel et al., 2014; Bony et al., 2020; Schiro
 53 et al., 2022). However, because many of the relevant small-scale processes are not resolved
 54 in climate models, it remains unclear how convective organization will evolve in a warmer
 55 climate.

56 While there are numerous ways by which convection may organize, one important
 57 mechanism is the clumping or clustering together of convective elements (e.g., Maddox,
 58 1980; Mapes, 1993; Bretherton et al., 2005). Such clustering occurs on a range of scales
 59 (Mapes & Houze, 1993), including at large scales that are resolved by climate models
 60 and at mesoscales that can typically only be resolved in high-resolution storm-resolving
 61 simulations. Recently, Bläckberg & Singh (2022) showed that the extent to which trop-
 62 ical precipitation exhibits clustering on the large scale increases with warming in climate
 63 projections from the Coupled Model Intercomparison Project phase 5 (CMIP5). This
 64 large-scale clustering is distinct from other types of organization on the mesoscale, but
 65 idealized simulations suggest that similar processes may act at both scales, and that both
 66 large-scale and mesoscale organization of convection may modulate the radiation bud-
 67 get (Wing et al., 2018).

68 Here we build on the work of Bläckberg & Singh (2022), showing that increased
 69 clustering of heavy precipitation with warming is a robust feature of the more recent CMIP6
 70 as well as CMIP5. Further, we explore the mechanisms that lead to large-scale cluster-
 71 ing of precipitation in the tropics and the influence of an increase in clustering on prop-
 72 erties of the atmosphere that are important for the radiation budget. The analysis will
 73 compare how clustering varies across different timescales, from interannual variability
 74 in both models and observations to changes in the climatological clustering of convec-
 75 tion in a warming climate. This approach allows us to assess whether observational con-
 76 straints of convective organization under current climate conditions can help constrain
 77 changes in organization and the associated radiative feedbacks with warming.

78 Previous studies have highlighted observed relationships between convective organi-
 79 zation and the tropical radiation budget. (Tobin et al., 2013; Holloway et al., 2017; Bony
 80 et al., 2020). For example, Bony et al. (2020) find tropical mesoscale convective organi-
 81 zation and Estimated Inversion Strength (EIS) in subsidence regions are the two strongest
 82 predictors of deseasonalized monthly anomalies in net top-of-atmosphere radiation, to-
 83 gether explaining about 60 percent of the variance. While the two predictors are signif-
 84 icantly correlated and potentially partly mechanistically connected (Williams et al., 2023),
 85 the authors find that both have an independent contribution in influencing the tropical
 86 radiation budget; EIS is found to have a stronger correlation with the cloudy component
 87 of the radiation budget while convective organization is found to have a stronger con-
 88 nection to the clear-sky component of the radiation budget. Bony et al. (2020) argue that
 89 clustering of deep convective elements is associated with a tropical-mean drying, result-
 90 ing in increased outgoing longwave radiation due to a reduction in the greenhouse effect.
 91 This hypothesis is supported by idealized studies of convective “self-aggregation” (e.g.,
 92 Wing & Emanuel, 2014). Both cloud-resolving and climate-model simulations run in ide-
 93 alized settings reminiscent of tropical conditions (i.e., low rotation rate and weak tem-
 94 perature gradients) show increased outgoing longwave radiation when convection is more
 95 clustered within the domain (Wing et al., 2018).

96 The preceding studies suggest that increased clustering of convection with warm-
 97 ing may lead to a negative clear-sky feedback from clustering-induced drying, resulting

98 in reduced equilibrium climate sensitivity (ECS) (Emanuel et al., 2014). However, re-
99 cent research suggests that clustering of deep convection on the large scale may also be
100 indirectly connected to a positive shortwave feedback on warming through changes in
101 low clouds (Schiro et al., 2022). According to this argument, drying associated with in-
102 creased clustering of convection is controlled by the large-scale overturning circulation
103 and is most pronounced in regions of climatological descent where low-cloudiness is sen-
104 sitive to changes in relative humidity. The associated cloud changes then lead to a net
105 positive feedback.

106 As the above discussion highlights, an important control on convective organiza-
107 tion at both large- and mesoscales comes from large-scale circulation patterns, includ-
108 ing the Intertropical Convergence Zone (ITCZ), the South Pacific Convergence Zone (SPCZ),
109 the Walker circulation, and convectively-coupled tropical waves (Bony et al., 2020; Quan
110 et al., 2025; Arnold & Randall, 2015; Wodzicki & Rapp, 2016; Wheeler & Kiladis, 1999).
111 Changes to the clustering of precipitation under warming may therefore be linked to, for
112 example, a “narrowing” of the ITCZ due to constraints on the export of energy by the
113 Hadley cell (Byrne & Schneider, 2016) or changes in the Walker circulation driven by
114 changes in zonal SST gradients (Quan et al., 2025), which may be associated with “El
115 Nino-like” shifts in the SST climatology (Watanabe et al., 2024).

116 In this study we explore how the spatial distribution of heavy precipitation changes
117 with increased large-scale clustering, demonstrating the importance of both meridional
118 contractions and zonal shifts in convection. We further show that the effect of large-scale
119 clustering on low clouds and moisture—key variables that control the radiation budget—
120 varies with timescale and between global climate models and observations, making it dif-
121 ficult to apply constraints from observed variability to a warmer climate. The paper is
122 structured as follows. First we describe the datasets used and our quantification of large-
123 scale clustering of precipitation (Section 2). Then we present the geographical spatial
124 patterns of heavy precipitation that are associated with a high level of clustering (Sec-
125 tion 3). After that, we connect the spatial patterns to leading mechanisms driving clus-
126 tering (Section 4). Finally, we present the moisture and low-cloud distribution associ-
127 ated with clustering (Section 5). Section 6 gives a summary of the key findings and an
128 outlook for future research.

129 **2 Data and Methods**

130 Our analysis is focused on variations in the large-scale clustering of heavy precip-
 131 itation in the tropics and its relationship to the atmospheric state in both observations
 132 and an ensemble of global climate models (GCMs) primarily from CMIP6. We begin by
 133 describing the datasets (both model and observational) used, before we describe the quan-
 134 tification of large-scale clustering, and our analysis framework.

135 **2.1 Models**

136 We use simulations from 27 GCMs from CMIP6 (Eyring et al., 2016), using data
 137 from the years 1970-1999 in the historical scenario, representing the current climate, and
 138 from the years 2070-2099 under Shared Socioeconomic Pathway 585 (SSP5-8.5), repre-
 139 senting a warmer climate. The models are chosen based on availability of the required
 140 variables and are shown in Figure 4. We use one ensemble member from each model.

141 In addition to the CMIP6 models, we also consider a simulation using a high-resolution
 142 GCM referred to here as IFS_9_FESOM_5 (Koldunov et al., 2023). The Deutsches Kli-
 143 marechenzentrum (DKRZ) Next Generation Earth Modelling Systems (NextGEMS) pre-
 144 final cycle provides high-resolution globally simulated atmospheric and oceanic variables
 145 for SSP3-7.0 forcing between 2025-2049 using the ECMWF Integrated Forecasting Sys-
 146 tem (IFS) at ~ 9 km horizontal grid spacing for the atmosphere and the Finite-VolumE
 147 Sea Ice-Ocean model version 2 (FESOM2) at 5 km horizontal grid spacing for the ocean
 148 (Koldunov et al., 2023). Although the model is at high resolution compared to the CMIP6
 149 models, it retains a convection parameterization, and we therefore describe it as a GCM
 150 rather than a storm-resolving model. Because the climate change signal during the sim-
 151 ulation is small, we only use the high-resolution GCM to characterize interannual vari-
 152 ability, using all available years.

153 **2.2 Observations**

154 Observed clustering of tropical precipitation is quantified based on daily precip-
 155 itation estimates from the National Oceanic and Atmospheric Administration Global Pre-
 156 cipitation Climatology Project (NOAA-GPCP) (Huffman et al., 2023), using the method
 157 described in the next subsection. We further use NOAA-GlobalTemp (Huang et al., 2024),
 158 and Clouds and the Earth's Radiant Energy System (CERES) data (NOAA Physical Sci-
 159 ences Laboratory, Climate Prediction Center, 2025) to provide observational estimates
 160 of surface temperature and outgoing longwave radiation, respectively. Estimates of ver-
 161 tical pressure velocity and specific and relative humidity are taken from the fifth gen-
 162 eration of the European Centre for Medium-Range Weather Forecasts reanalysis (ERA5)
 163 (Hersbach et al., 2023). Apart from precipitation, all variables are taken as monthly av-
 164 erages.

165 Finally, we develop a simple estimate of the low-cloud fraction using the tropical
 166 weather states defined in Tselioudis et al. (2010) based on data from the International
 167 Satellite Cloud Climatology Project (ISCCP) (Young et al., 2018). Tselioudis et al. (2010)
 168 used a clustering algorithm to categorize histograms of cloud-top pressure and optical
 169 thickness given by the ISCCP D1 dataset into a series of weather states defined in three
 170 hourly polar-orbiting satellite scans with daily global coverage on a $1^\circ \times 1^\circ$ grid. Each
 171 weather state is characterized by a histogram in cloud-top pressure and optical thick-
 172 ness that represents the centroid over all members of that weather state. Here we esti-
 173 mate the cloud fraction as a function of pressure for a given weather state as the total
 174 frequency of clouds of all optical thicknesses in a given range of cloud-top pressure within
 175 the corresponding centroid histogram. We then calculate the low-cloud fraction LCF_i
 176 of weather state i as the total cloud fraction below 600 hPa. The monthly low-cloud frac-

177 tion is then taken as

$$LCF = \sum_i f_i LCF_i, \quad (1)$$

178 where f_i is the frequency of weather state i over the month in question.

179 As described further below, all observational datasets are regredded conservatively
 180 to a common $2.8^\circ \times 2.8^\circ$ grid for analysis. We use observations covering the time pe-
 181 riod between 1998-2023 for all datasets, except for cloud fraction (based on ISCCP), which
 182 is limited to 1998-2017.

183 2.3 Quantifying Large-Scale Clustering of Heavy Precipitation

184 We quantify clustering of precipitation following Bläckberg & Singh (2022) using
 185 daily surface precipitation in the tropics (30°S - 30°N). To facilitate the comparison of clus-
 186 tering across different models and the observations, we first interpolate the daily precipi-
 187 tation to a $2.8^\circ \times 2.8^\circ$ grid using a first-order conservative method (Jones, 1999) to pre-
 188 serve tropical-mean properties from the native grid. Next we define heavily precipitat-
 189 ing regions as gridboxes for which the precipitation rate exceeds a threshold. The thresh-
 190 old is calculated as the 95th spatial percentile of daily precipitation over all gridboxes
 191 in the tropics temporally averaged over the 30-year climatology (or 25-year in the case
 192 of observations). For the GPCP observations, this threshold is 16 mm day^{-1} . Distinct
 193 heavy precipitation features are identified as 8-connected contiguous regions of precipi-
 194 tation exceeding the threshold or single grid boxes if there are no neighboring connec-
 195 tions.

196 We define our primary measure of clustering, A_m , as the mean area of heavy pre-
 197 cipitation features over the entire tropics. A_m conceptually captures clustering by dis-
 198 tinguishing scenes with many small precipitation features and scenes where precipita-
 199 tion is aggregated into fewer and/or larger precipitating features (Figure 1). The mean
 200 area of features, A_m , was chosen due to its interpretability, however, we note that it is
 201 only one aspect of the large-scale organization of precipitation, and A_m does not describe
 202 important spatial characteristics such as the total area, shape, proximity, gradients of
 203 precipitation intensity, and location of precipitation features. A number of other mea-
 204 sures of large-scale clustering are analyzed and their interrelationship is presented in Fig-
 205 ures S1-4 in the supporting information.

206 An important aspect of our method is that, by definition, regions of heavy precip-
 207 itation occupy 5% of the domain on average. Thus when comparing two climates, the
 208 mean area fraction of heavy precipitation \bar{A}_f remains constant. Differences in the mean
 209 area of features, A_m , between climates are entirely due to a reorganization of precipi-
 210 tation, and changes in A_m are inversely related to the mean number of precipitation fea-
 211 tures. However, the above constraint does not apply to the precipitation distribution dur-
 212 ing a given month. Indeed, as we shall see, an important driver of variations in tropi-
 213 cal precipitation clustering in interannual variability is the area fraction of precipitation,
 214 A_f . We therefore consider the behavior of both the mean area of heavy precipitation fea-
 215 tures, A_m , and the area fraction of heavy precipitation, A_f , in our analysis below.

216 2.4 Describing Relationships to Large-Scale Clustering of Heavy Pre- 217 cipitation

218 Having quantified large-scale precipitation clustering, we seek to characterize the
 219 relationships between such clustering and other large-scale climate variables. Specifically,
 220 we consider these relationships for interannual variability in both models and observa-
 221 tions, and for changes in climate across the CMIP6 ensemble. Throughout, we define in-
 222 terannual variability in a given variable by deseasonalized monthly anomalies, calculated
 223 as the monthly-mean anomaly from the climatology of the associated month after de-

trending the time series. The trend is estimated by a first-order linear least squares regression of the data at each location from the daily (precipitation-based metrics) or monthly (all other metrics) time series.

As we will see, for interannual variability, the mean area of features, A_m , and the area fraction of precipitation, A_f , are strongly correlated with each other and to the large-scale climatic state. To estimate the individual effect of A_m , we apply the method of Pearson partial correlation (Mardia et al., 1979). The partial correlation $r(X, Y|Z)$ represents the relationship between variables X and Y after the removal of the effect of Z , and is given by

$$r(X, Y|Z) = \frac{r(X, Y) - r(X, Z)r(Y, Z)}{\sqrt{1 - r^2(X, Z)}\sqrt{1 - r^2(Y, Z)}}, \quad (2)$$

where $r(X, Y)$ is the regular correlation between X and Y . The significance of partial correlations is evaluated using the standard t-test for partial correlations.

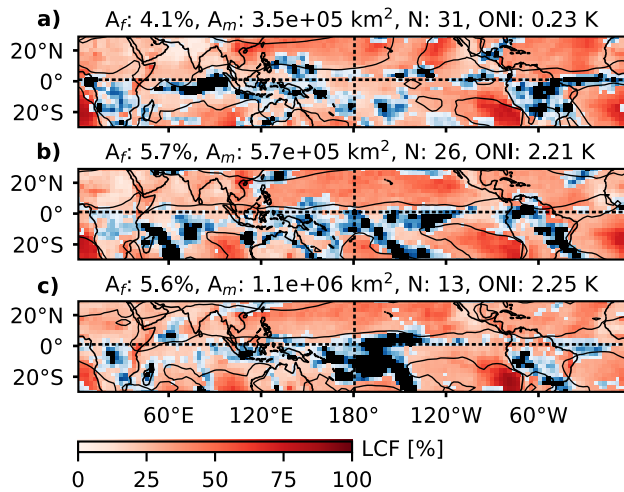


Figure 1. February daily snapshots of GPCP precipitation (blue colors) and regions of heavy precipitation (black shading) with monthly contour of ERA5 500 hPa relative humidity representing the median over the tropics (black line) and monthly ISCCP low cloud fraction (red colors). The panel titles show the total area of heavy precipitation as a fraction of the tropical domain area (A_f), the mean area (A_m) and number (N) of heavy precipitation features, and the Oceanic Niño Index (ONI) taken from NOAA-GlobalTemp. From (a-c), clustering increases according to A_m . The clustering from (a-b) is primarily due to an increase in A_f , whereas the clustering from (b-c) is primarily due to the closer proximity of heavy precipitation to the central Pacific.

235 3 Spatial Patterns of Heavy Rainfall Clustering

236 The purpose of this section is to elucidate the spatial patterns of precipitation that
 237 produce a high degree of clustering. We first consider how clustering changes in inter-
 238 annual variability before we investigate the spatial patterns associated with strong in-
 239 creases in clustering with warming across the CMIP6 ensemble.

240 Figure 2 shows the regression of monthly anomalies in the frequency of occurrence
 241 of heavy precipitation, C , onto the mean area of heavy precipitation features, A_m , for
 242 the observations. When tropical precipitation is observed to be highly clustered on the
 243 large scale, heavy precipitation tends to occur more frequently in the central equatorial
 244 Pacific. Figure 2 is calculated for all months, but similar spatial patterns can be seen
 245 in individual months, strongest in DJF (Figure S5 in the supporting information). Other
 246 notable spatial characteristics of the regression include a decrease in heavy precipitation
 247 over the maritime continent and a small but statistically significant (crosses) decrease
 248 in heavy precipitation over the Amazon and Atlantic.

249 To quantify the shift of heavy precipitation to the central equatorial Pacific, we de-
 250 fine the distance metrics C_z , which represents the mean distance of heavily precipitat-
 251 ing points within the tropics to the meridian given by the longitude 180°E , and C_m , which
 252 represents a similar metric defined based on distance to the equator. These are some-
 253 what arbitrary zonal and meridional reference lines with which to describe the zonal and
 254 meridional shifts, and the clustering redistribution of heavy precipitation may be bet-
 255 ter characterized relative to the climatological distribution. For example, in most mod-
 256 els, with warming heavy precipitation moves south relative to the northern hemisphere
 257 climatological convergence zone or north relative the climatological SPCZ or both. How-
 258 ever, for simplicity, we use C_z and C_m defined based on 180°E and the equator.

259 As expected from the regression map, there is a strong relationship between the
 260 mean area of features, A_m , and C_z (Figure S2 in the supporting information). However,
 261 as shown in Figure 3a, there is also a strong observed relationship in interannual vari-
 262 ability between A_m and the total area fraction of heavy precipitation, A_f [$r^2(A_f, A_m) \sim$
 263 0.7], with greater A_f favoring greater A_m . This suggests a large part of the observed re-
 264 gression pattern is due to the effect of changes in the total precipitating area, rather than
 265 a pure spatial redistribution of a fixed number of heavily precipitating points. This com-
 266 plicates the interpretation of increased clustering in internal variability, since when com-
 267 paring climates, the mean area fraction of heavy precipitation \bar{A}_f remains fixed at 0.05.
 268 To address this, we estimate the variations in the distribution of heavy precipitation that
 269 contribute to variations in A_m independent of changes in A_f using Pearson partial corre-
 270 lation (see Methods).

271 Both C_z and C_m are negatively correlated with the mean area of heavy precipi-
 272 tation features, A_m , when the effect of changes in the area fraction of heavy precipi-
 273 tation, A_f , is removed (star in Figure 3b), suggesting that there is a shift of convection
 274 toward the equator and the central Pacific when the tropics are highly clustered. For a
 275 given A_f , this contraction of heavily precipitating regions explains about 5-10 percent
 276 of the remaining variance after the effect of changes in A_f is removed.

277 Both the CMIP ensemble and the high-resolution model generally show similar spa-
 278 tial patterns associated with increasing large-scale clustering (Figure 3b and Figure S6a-
 279 b in the supporting information). All models show significant relationships between A_m
 280 and A_f , although generally somewhat weaker than in observations, and most models show
 281 significant negative partial correlations between the distance metrics C_z (24/27 CMIP6
 282 models) and C_m (22/27 CMIP6 models) after removing the effect of changes in A_f (Fig-
 283 ure 3b). That is, as for the observations, most models agree that higher clustering, as
 284 measured by a larger mean area of heavy precipitation features, is associated with a shift
 285 in convection toward the central equatorial Pacific. Interestingly, the high-resolution GCM

²⁸⁶ did not show a significant partial correlation with C_m , suggesting clustering in that model
²⁸⁷ is not sensitive to the meridional contraction of heavy precipitation to the equator.

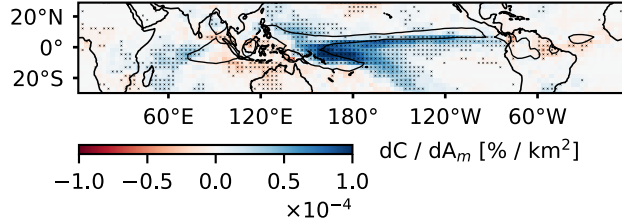


Figure 2. GPCP frequency of occurrence of heavy precipitation, C , regressed onto the mean area of heavy precipitation features, A_m , for interannual variability. The contour shows the 90th percentile of the climatological C and crosses indicate whether correlations are statistically significant.

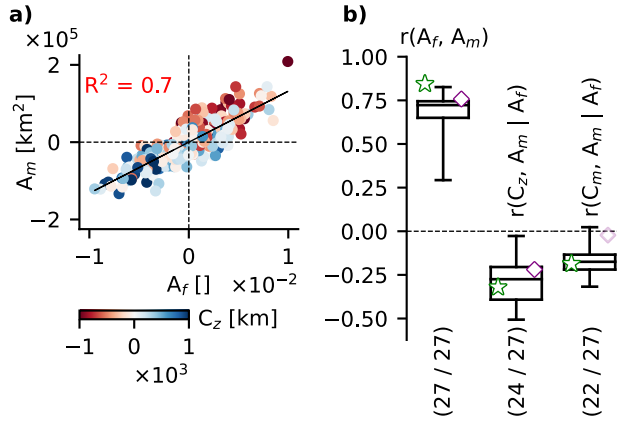


Figure 3. Scatter plot of monthly anomalies in area fraction of heavy precipitation, A_f , and the mean area of heavy precipitation features, A_m , colored by the zonal proximity of heavy precipitation to the longitude 180° E in the central pacific, C_z , for GPCP observations (a). Boxplot of the correlations between A_f and A_m and partial correlations of C_z and the proximity of heavy precipitation to the equator, C_m , with A_m outside the influence of A_f for the CMIP6 ensemble (b). The fraction of CMIP models with statistically significant correlations is indicated below each box, and the GPCP (star) and high-resolution GCM (diamond) correlations are shown in lighter colors if not statistically significant.

We now consider how large-scale clustering of heavy precipitation changes under climate change. Bläckberg & Singh (2022) noted that large-scale clustering increases as the climate warms in projections of climate change by the CMIP5 ensemble. Figure 4a shows that this is also true for CMIP6; all models project an increase in A_m with warming to varying degrees. However, there is a wide spread in climatological A_m and wide spread in climatological increase in A_m across the ensemble, suggesting the degree of large-scale clustering and the change in large-scale clustering with warming is poorly constrained in the models.

Given the climatologically fixed A_f in this framework, changes in the mean area of precipitation features, A_m , with warming are driven entirely by a spatial reorganization of convection to larger features. The present analysis evaluates whether the spatial patterns associated with a high degree of clustering of precipitation in interannual variability may also be relevant to the redistribution of heavy precipitation causing increased clustering under warming. Indeed, all but one model show a reduction in C_m with warming, indicating a contraction of heavy precipitation towards the equator (Figure 4b). Further, all models contract heavy precipitation towards the hydrological equator, or "ITCZ center", which is defined here as the latitude of highest specific humidity at 700 hPa as a function of longitude and time in months (Figure 4c). One possible interpretation of this is that a narrowing of the ITCZ provides a mechanism for the overall increase in clustering with warming. However, we note that the change in C_m with warming is uncorrelated with the change in A_m across the CMIP6 ensemble; models exhibiting stronger ITCZ narrowing with warming do not show stronger increases in large-scale clustering of precipitation. On the other hand, there is a significant correlation between increases in mean area of precipitation features, A_m , and changes in C_z across the CMIP6 ensemble. That is, models that show a greater clustering with warming also show a more zonal shift of heavy precipitation to the central Pacific (note that the zonal and meridional contractions are somewhat anticorrelated, as also identified by Popp & Bony (2019)).

Going beyond the simple distance metrics, Figure 5 regresses the projected increase in frequency of occurrence of heavy precipitation onto the projected increase in A_m across the CMIP ensemble. This reveals a spatial pattern of precipitation changes with several similarities to the pattern for interannual variability shown in Figure 2. However, an important distinction is that, for changes with warming, the redistribution of heavy precipitation is a conserved property, due to the climatologically fixed A_f . Similarities between the regression patterns include a regression coefficient largest in the central Pacific close to the equator, and a redistribution of precipitation away from the maritime continent, Amazon, and Atlantic. While under interannual variability heavy precipitation shifts southward in the Pacific for highly clustered states, the changes with warming show a northward shift of heavy precipitation in the Pacific.

We note that the spatial patterns associated with a climatologically high degree of clustering of heavy precipitation across the CMIP6 ensemble are rather different from those of internal variability and changes with warming (Figure S6c in the supporting information). Models with high climatological values of A_m tend to have more convection in the warm pool, over tropical continents, and at the edges of the northern and southern convergence zones over the Pacific Ocean. These relationships cannot be summarized by a single value of either C_z or C_m . Rather, we find that high climatological values of A_m are associated with high month-to-month variability in A_f . This indicates that high spatial clustering also corresponds to high clustering in time, with some days producing a large amount of heavy precipitation across the tropics and other days producing much less.

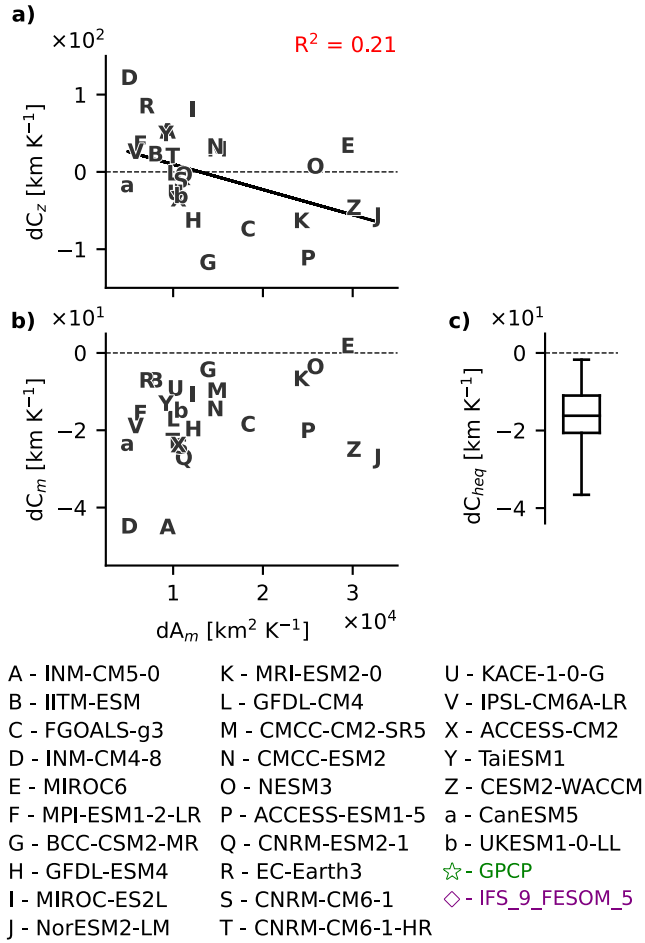


Figure 4. Scatter plot of change in climatological mean area of heavy precipitation features, A_m , with change in climatological mean distance of heavy precipitation to the central pacific, C_z , (a) and change in mean heavy precipitation proximity to the equator, C_m (b). Boxplot of change in climatological mean distance to the hydrological equator, C_{heq} , (c) where the hydrological equator is defined as the latitude of highest specific humidity at 700 hPa as a function of longitude and time in months. All quantities are normalized by the tropical surface temperature warming from the historical to the SSP585 scenario simulation period in CMIP6 models.

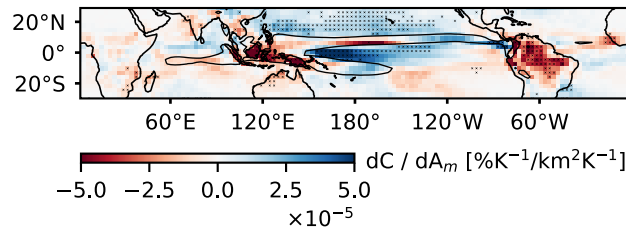


Figure 5. Increase in frequency of occurrence of heavy precipitation, C , regressed onto increase in A_m per kelvin tropical warming from the historical to the SSP585 scenario simulation period across the CMIP6 ensemble. Contour shows the ensemble-mean 90th percentile of C in the historical period and crosses indicate whether correlations are statistically significant.

337 In summary, the spatial patterns of heavy precipitation associated with highly clustered
338 states vary across timescales, but there are important common threads. In both
339 internal variability and for changes with warming, higher clustering as measured by A_m
340 is associated with more heavy precipitation in the central equatorial Pacific. In partic-
341 ular, models with stronger increases in large-scale clustering of precipitation under warm-
342 ing also exhibit greater zonal shifts in convection to the central Pacific. This potentially
343 suggests the Walker circulation, and the East-West SST gradient in the Pacific, as an
344 important control on the magnitude of changes in large-scale clustering of precipitation
345 with warming. We next investigate the relationships between SST changes and changes
346 in A_m in both internal variability and under climate change.

347 4 SST Drivers of Heavy Rainfall Clustering

348 This section investigates the extent to which changes in the El Niño-Southern Os-
 349 cillation can explain changes in clustering across timescales. We use the Oceanic Niño
 350 Index (ONI; Sobel et al., 2002) to identify the state of the El Niño-Southern Oscillation
 351 in interannual variability. The ONI represents the three-month rolling average SST anomaly
 352 in the Niño3.4 region (5°S - 5°N , 120° - 170°W), calculated here relative to the full range
 353 of years used in the climatology. ONI values greater than 0.5°C represent El Niño con-
 354 ditions and ONI values less than -0.5°C represent La Niña conditions. The climatolog-
 355 ical East-West Pacific SST gradient, defined as the time-mean difference between the SST
 356 in the western- (5°S - 5°N , 80° - 150°E) and eastern (5°S - 5°N , 180° - 80°W) Pacific boxes,
 357 which we denote T_z , serves as an indicator for climatologically “El Niño-like” conditions
 358 (Watanabe et al., 2024).

359 Observations show several indications that highly clustered states, corresponding
 360 to large values of the mean area of heavy precipitation features, A_m , are associated with
 361 El Niño-like conditions. Firstly, SST regressed onto A_m for interannual variability shows
 362 a pattern strongly reminiscent of an El Niño SST signature (Alexander et al., 2002) (Fig-
 363 ure 6). Secondly, during times of ONI exceeding 0.5°C compared to all days, A_m increases
 364 as heavy precipitation moves from the maritime continent towards the central Pacific
 365 (Figure S7b in supporting information). Finally, independent of changes in A_f , ONI shows
 366 a positive partial correlation with A_m (Figure 7a). Most CMIP models capture the ob-
 367 served connection between ONI and A_m (Figure S1 in the supporting information) and
 368 the independent contribution of ONI on A_m outside the influence of A_f , as does the high-
 369 resolution GCM (Figure S3 in the supporting information and Figure 7b). Thus both
 370 models and observations show that large-scale clustering of precipitation is stronger dur-
 371 ing El Niño than La Niña. This is despite the fact that El Niño represents a weakening
 372 of the Walker circulation and a weakening of tropical SST gradients, both of which are
 373 generally thought to facilitate the organization of convection on large scales.

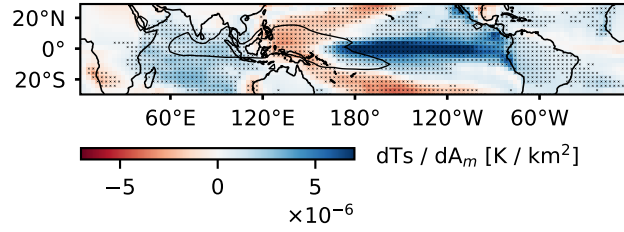


Figure 6. NOAA-GlobalTemp surface temperature, T_s , regressed onto A_m for interannual variability. The contour shows the climatological 90th percentile of T_s , and crosses indicate whether correlations are statistically significant.

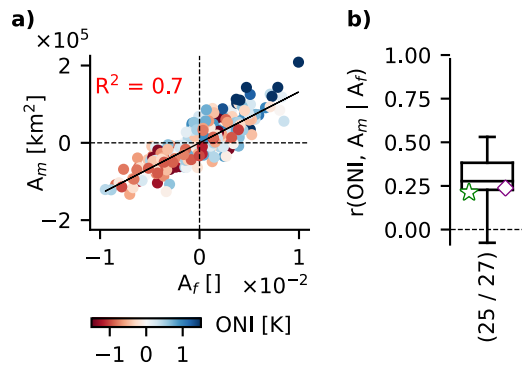


Figure 7. Same as Figure 3, but with the Oceanic Niño Index (ONI) in scatter colors and as explanatory variable in boxplot.

The strong connection between El Niño conditions and A_m in interannual variability motivates the investigation of changes in the climatological Pacific SST gradient to a more El Niño-like state as a mechanism for explaining model-spread in projected changes to clustering. Consistent with expectations, the magnitude of the weakening of the East-West Pacific SST gradient explains a similar amount of variance in projected changes in clustering as the zonal shift in heavy precipitation (Figure 8). Models that have more El Niño-like warming patterns tend to exhibit larger increases in large-scale clustering of precipitation. Regressing the SST changes against projected changes in the mean area of precipitation features, A_m , also shows an El-Niño-like pattern, with a relative warming in the east and relative cooling in the west (Figure 9). In addition, the regression pattern has a noticeable north-south gradient, consistent with the positive regression coefficients for heavy precipitation frequency north of the equator in Figure 5.

We have shown that El Niño-like states tend to result in a higher degree of clustering in both interannual variability and across the CMIP6 ensemble under climate change. Note, however, that there are changes in the zonal SST gradient, T_z , and the mean distance of heavy precipitation to the central Pacific of both signs across the 27 CMIP6 models we analyse, suggesting that zonal shifts in convection are not the primary reason for the ensemble-mean increase in large-scale clustering with warming that we document. We hypothesize that the ensemble-mean increase in A_m is instead associated with a meridional shift in convection, potentially related to a narrowing of the ITCZ (Byrne & Schneider, 2016). All but one model exhibit negative changes in C_m with warming, and this is associated with an increase in the large-scale clustering of precipitation in natural variability.

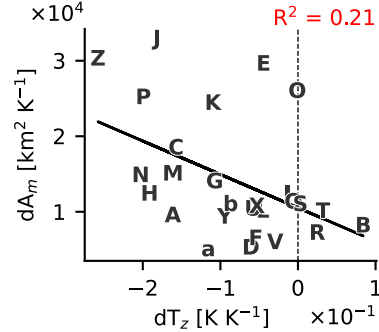


Figure 8. Same as Figure 4a, but with the change in the climatological Pacific SST gradient, T_z , per Kelvin tropical warming as explanatory variable. Models are as given in the legend in Figure 4.

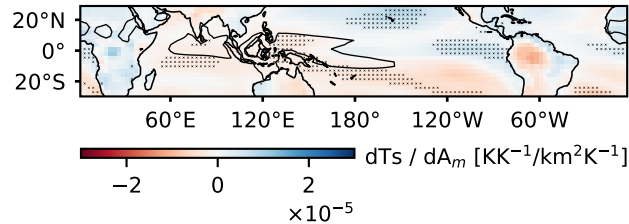


Figure 9. Change in surface temperature, T_s , regressed onto change in mean area of heavy precipitation features, A_m , per Kelvin tropical warming from the historical to the SSP585 scenario simulation period across the CMIP6 ensemble. Contour shows ensemble-mean 90th percentile climatological T_s and crosses indicate if correlations are statistically significant.

5 The Effect of Heavy Rainfall Clustering on Clouds and Humidity

We now consider how large-scale clustering of precipitation influences the cloud and humidity distribution. Our motivation is to understand how such clustering may influence radiative feedbacks. Previous authors have found that the degree of clustering on different spatial scales has an effect on the radiation budget and clouds (e.g., Bony et al., 2020; Wing & Emanuel, 2014; Pendergrass et al., 2016). The literature suggests changes in clustering under warming may lead to different cloud feedbacks and may therefore affect equilibrium climate sensitivity (ECS) (Schiro et al., 2022). This section investigates this hypothesis for large-scale clustering across the CMIP6 ensemble. As for previous sections, the analysis assesses whether relationships in interannual variability can be used to infer the response to climate change, raising the possibility of an observational constraint on particular radiative feedbacks or ECS itself.

Rather than focusing on changes in radiative fluxes or calculating feedback strength directly, we focus on changes in mid-tropospheric relative humidity, which has been argued to cause a negative longwave feedback associated with changes in convective organization (Tobin et al., 2013; Bony et al., 2020), and changes in low-cloud fraction in regions of subsidence, which have been argued to cause a positive shortwave feedback associated with changes in convective organization (Schiro et al., 2022). Changes in low clouds in regions of subsidence are also known to be important for understanding model spread in ECS (Zelinka et al., 2020). Correlations between measures of large-scale clustering of heavy precipitation and various other metrics commonly used to assess changes to the radiation budget on interannual and climatological timescales are presented in Figure S1-4 in the supporting information.

For our analysis, the mid-tropospheric relative humidity, RH, is taken as the 500 hPa value, but the conclusions are not sensitive to using proximate pressure levels down to 700 hPa. Observed low-cloud fraction, LCF, is calculated using the ISCCP weather states (Tselioudis et al., 2010) as described in Section 2.2, and taken as the cloud fraction below 600 hPa. CMIP6 low-cloud fraction is calculated analogously, with cloud fraction pre-processed by interpolating hybrid-sigma coordinates to 19 pressure levels if not already available on pressure levels. We also consider the mean low-cloud fraction in regions of descent, denoted by a subscript d and calculated as the mean of gridpoints for which the monthly-mean vertical pressure velocity at 500 hPa is positive. Later we will consider variables in regions of ascent, defined analogously for negative 500 hPa vertical velocity and identified by a subscript a .

Figure 10a and Figure 11a show observational estimates of the regression patterns of RH and LCF against the mean area of precipitation features, A_m , for interannual variability. The regressions show a clear El-Niño-like pattern, with increases in RH and decreases in LCF in the central and eastern Pacific, and opposite changes over the warm pool. This suggests the changes in RH and low clouds with increased tropical clustering are caused at least in part by variations associated with El Niño-Southern Oscillation.

From a tropics-wide perspective, when the observed degree of clustering is high according to A_m , the tropical mean is drier (Figure 10b) while LCF increases, both when averaged over descending grid points (LCF_d in Figure 11b) and in regions of time-mean descent (contour on Figure 11a). The environmental signature associated with large-scale clustering is therefore consistent with a negative longwave feedback identified for large-scale clustering in idealized simulations (Arnold & Randall, 2015) and a longwave- and low-cloud cooling signature found associated with interannual variations in mesoscale organization (Bony et al., 2020).

However, partial correlations of A_m with RH excluding the influence of the total area fraction of heavy precipitation, A_f , are insignificant in the observations (Figure 10b).

448 This suggests that the influence of A_m on relative humidity is almost entirely due to in-
 449 creasing A_f . Observed correlations of relative humidity and the distance metrics C_m and
 450 C_z , representing proximity of heavy rainfall to the equator and the central Pacific, re-
 451 spectively, are also generally insignificant. Observed LCF_d on the other hand increases
 452 for all three forms of spatial clustering, outside the influence of A_f (Figure 11b).

453 The CMIP6 ensemble generally agrees on the strong association between A_f and
 454 the aforementioned tropical environmental signatures. However, unlike the observational
 455 estimates, about half of the models also show a significant relationship between relative
 456 humidity and spatial shifts of heavy precipitation (Figure 10b). In particular, in a sub-
 457 set of models, zonal shifts in heavy precipitation to the central Pacific are (independent
 458 of variations in A_f) associated with a moistening in the tropics, while meridional shifts
 459 to the equator result in domain-mean drying. These relationships are also present in the
 460 high-resolution GCM. The models generally do not capture the observed LCF_d signa-
 461 ture for clustering outside the influence of A_f , except for a subset of CMIP models pro-
 462 ducing increases in LCF_d for meridional shifts in heavy precipitation (Figure 11b).

463 Other notable independent effects of the spatial preference of heavy precipitation
 464 on environmental conditions include a reduction in high cloud fraction above 400 hPa
 465 in regions of ascent, HCF_a , with meridional shifts in precipitation ($r(C_m, HCF_a | A_f) \sim$
 466 0.25 in observations, the high-resolution GCM, and the model-mean of CMIP model cor-
 467 relations).

468 Our analysis of interannual variability has revealed strong relationships between
 469 RH and low-cloud fraction and large-scale clustering of precipitation in observations. How-
 470 ever, in observations, the RH relationships are primarily driven by changes in the area
 471 fraction of convection A_f . A_f also influences low cloud fraction, LCF_d , but spatial shifts
 472 in heavy precipitation retains a connection to LCF_d outside the influence of A_f in ob-
 473 servations. We now consider relationships between RH and low-cloud fraction changes
 474 and changes in the clustering of precipitation in climate projections.

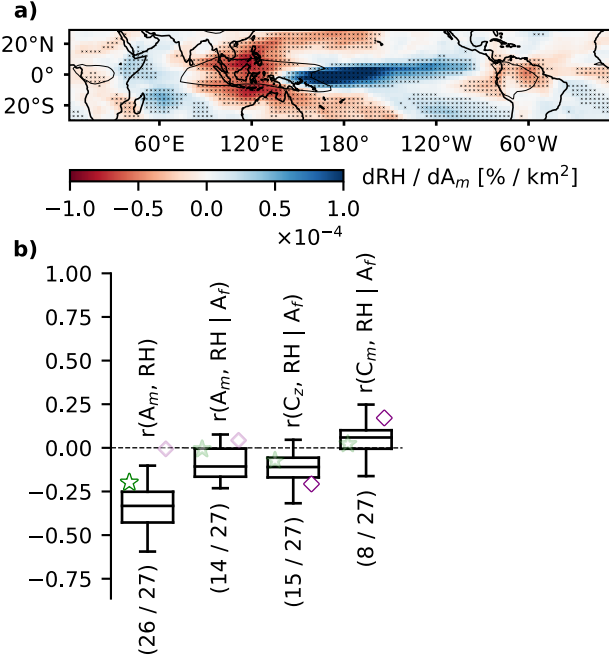


Figure 10. Relative humidity at 500 hPa, RH, regressed onto mean area of heavy precipitation features, A_m , in interannual variability (a). Boxplots of correlations and partial correlations outside the influence of the total area of heavy precipitation, A_f , of RH and A_m , mean distance of heavy precipitation to 180°E , C_z , and mean distance of heavy precipitation to the equator, C_m (b). Star and diamond show results for observations and high-resolution GCM, respectively, shown in lighter colors if not statistically significant. The numbers below the boxplots gives the fraction of models with statistically significant correlations.

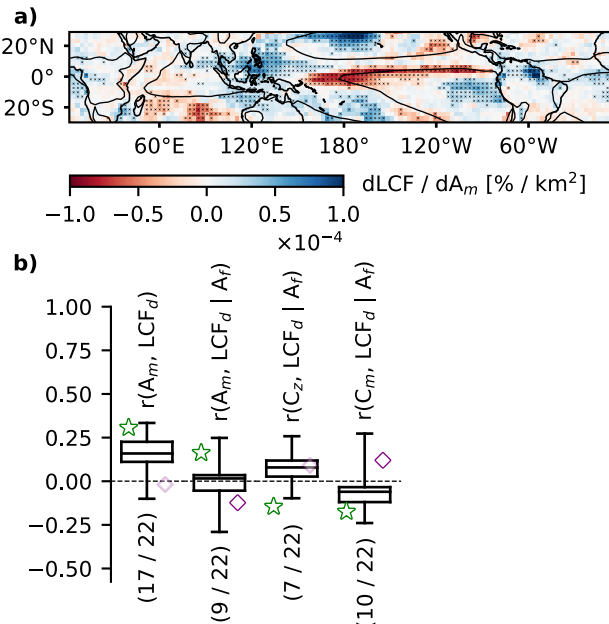


Figure 11. Same as Figure 10, but with the low cloud fraction, LCF, and low cloud fraction in regions of descent, LCF_d , as response variable.

475 Consistent with the results from the previous section, models with larger increases
 476 in large-scale clustering under warming tend to have changes in relative humidity and
 477 clouds consistent with an El Niño-like shift in the tropical circulation. The regression
 478 patterns of RH and LCF onto changes in A_m under warming across the CMIP6 ensemble
 479 (Figure S10a-b) are similar to those for interannual variability presented above. How-
 480 ever, in contrast to the case for interannual variability, changes in large-scale clustering
 481 with warming have little connection to changes in tropical-mean mean RH or low-cloud
 482 fraction in regions of descent, LCF_d , across the CMIP6 ensemble (Figure 12a, b). Given
 483 this, it is perhaps not surprising that there is no correlation between the increase in A_m
 484 within a model under warming and the model's ECS (Figure 12c). Here we take ECS
 485 from the supplementary material of Zelinka et al. (2020) and Hausfather et al. (2022).

486 The results therefore indicate that changes in large-scale clustering under warm-
 487 ing do not strongly affect radiative feedbacks, despite indications from observations that
 488 more clustered states are drier with more low-clouds in regions of large-scale descent. One
 489 reason for this result appears to be the different ways in which large-scale clustering can
 490 manifest at different timescales. In interannual variability, increases in clustering are as-
 491 sociated with increases in the fractional area of heavy precipitation, defined here by A_f .
 492 Under climate change, increases in A_f in one month must be balanced by decreases in
 493 another month such that the overall average must remain constant. When the effects of
 494 changes in area fraction are removed, the observed relationship to RH becomes weak.
 495 However, this explanation is not the whole story, as many of the models do exhibit changes
 496 in RH associated with increased clustering independent of changes in the area fraction
 497 of heavy precipitation. Even among this subset of models, however, future increases in
 498 A_m are not a good predictor of future changes in clouds or relative humidity. This sug-
 499 gests that caution should be used in extrapolating relationships—either observed or simulated—
 500 between large-scale clustering and other properties of the climate in internal variability
 501 to those for climate change.

502 Finally, we note that there does exist a relationship between a tropical-mean dry-
 503 ing and the proximity of heavy rainfall to the equator. Under warming, variations in the
 504 meridional contraction of heavy rainfall, as measured by the mean distance of heavily
 505 precipitating gridpoints to the equator C_m , explain about 45 percent of the variance in
 506 tropical-mean drying (Figure 13 and Figure 14). This relationship is consistent with the
 507 sign of the relationship between RH and C_m in interannual variability in a subset of CMIP6
 508 models (Figure 10b). This result potentially highlights the importance of ITCZ narrow-
 509 ing as a specific manifestation of large-scale clustering that appears to be important for
 510 setting the tropical-mean relative humidity. However, we note that most of the spread
 511 in projected drying is due to the result of four models with dramatically different dry-
 512 ing trends, and thus further work is required to confirm if this relationship is robust and
 513 physical.

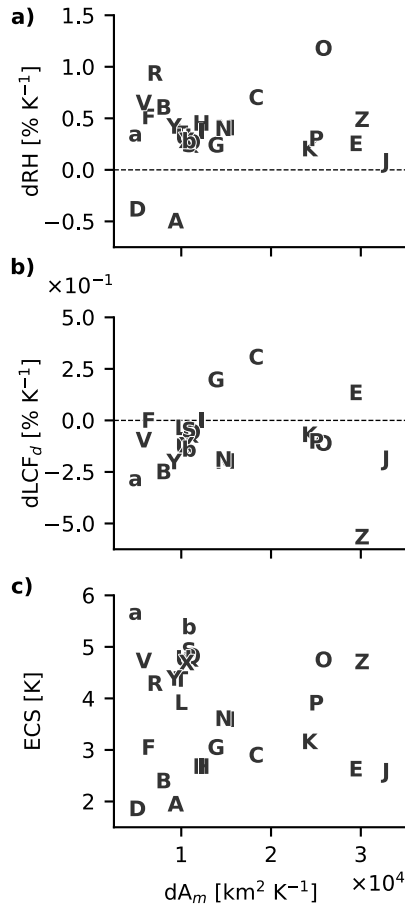


Figure 12. Scatter plot of change in A_m between historical period and SSP585 period per Kelvin tropical warming and associated tropical-mean change in 500 hPa relative humidity, RH, (a), low cloud fraction in regions of descent, LCF_d (b), and equilibrium climate sensitivity (ECS) in the CMIP6 ensemble (c). Models are as given in the legend in Figure 4.

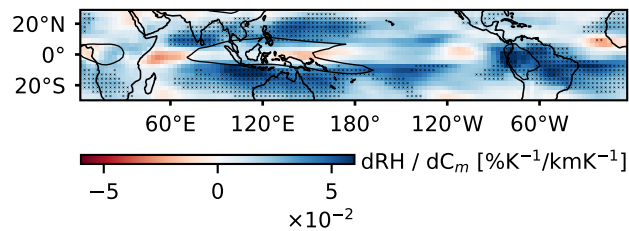


Figure 13. Change in relative humidity at 500 hPa, RH, regressed onto changes in mean distance of heavy precipitation to the equator, C_m between the historical and SSP585 periods per Kelvin warming.

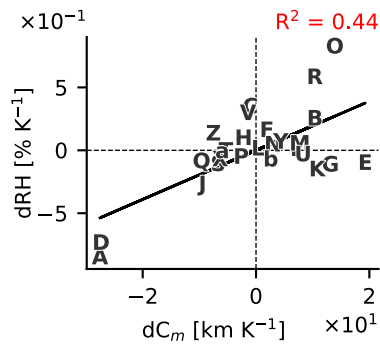


Figure 14. Scatter plot of change in mean distance of heavy precipitation to the equator, C_m , between historical period and SSP585 period per Kelvin tropical warming and associated tropical-mean change in 500hPa relative humidity, RH. The values are plotted as anomalies from the ensemble mean and models are as given in the legend in Figure 4.

514 **6 Summary and Discussion**

515 In this paper we have (1) presented the dominant spatial patterns of heavy pre-
 516 cipitation that produce a high degree of clustering on the large scale (Section 3); (2) tied
 517 the associated spatial patterns to mechanisms driving clustering through large-scale SST
 518 patterns (Section 4); and (3) evaluated the associated changes in properties of the at-
 519 mosphere that are important for the radiation budget (Section 5) in both interannual
 520 variability and for projected changes with warming. We have defined the degree of clus-
 521 tering of precipitation based on the spatial distribution of the top 5 percent heaviest daily
 522 rainfall instances, with high clustering corresponding to scenes in which the mean area
 523 of individual precipitation features is large. A challenge in any definition of convective
 524 organization is in how one measures organization consistently as the total amount of pre-
 525 cipitation changes (Retsch et al., 2020; Tobin et al., 2013). In the present study, the use
 526 of a percentile precipitation threshold accounts for changing mean precipitation rates in
 527 different climates. However, in internal variability, the area of precipitation features is
 528 affected by both spatial shifts in the precipitation distribution and variations in the to-
 529 tal area fraction of heavy precipitation, A_f . This is addressed here by using Pearson par-
 530 tial correlations to evaluate the independent contributions of different measures of the
 531 spatial distribution of precipitation while controlling for the effect of A_f .

532 When tropical precipitation is observed to be highly clustered on the large scale
 533 in interannual variability, heavy precipitation gravitates meridionally to the equator and
 534 zonally towards the central Pacific. In climate projections, large-scale clustering of pre-
 535 cipitation is found to increase in all models, and this coincides with a shift of precipi-
 536 tation toward the equator across the ensemble. We therefore hypothesize that a narrow-
 537 ing of the ITCZ may be an important contributor to increases in large-scale clustering
 538 of precipitation under warming. This implicates mechanisms related to the transport of
 539 energy by the Hadley circulation that have been argued to control changes in ITCZ width
 540 (Byrne & Schneider, 2016).

541 On the other hand, the intermodel spread in changes in clustering with warming
 542 across the CMIP6 ensemble is related to zonal rather than meridional shifts in the pre-
 543 cipitation. This motivated an investigation of the role played by Pacific SST gradients
 544 in changes in large-scale clustering of precipitation. In interannual variability, El Niño-
 545 Southern Oscillation linked variability appears to be a major driver of variability in large-
 546 scale clustering of precipitation, with precipitation during El Niño events more clustered
 547 than during La Niña events.

548 Under warming, changes in zonal SST gradients appeared to explain the sensitiv-
 549 ity of projected clustering to zonal shifts in heavy rainfall; those models with more El
 550 Niño-like warming patterns tended to exhibit stronger increases in precipitation cluster-
 551 ing. This is important given the large disagreement between observed and simulated SST
 552 trends in the topical Pacific (e.g., Wills et al., 2022). Observations show a strengthen-
 553 ing of the SST gradient, suggesting a weaker increase in large-scale clustering compared
 554 to simulations, which tend to show a weakening of tropical SST gradients.

555 Finally, we assessed if the changes in clustering with warming may have an influ-
 556 ence on climate sensitivity. In observed interannual variability, a greater area fraction
 557 of heavy precipitation, A_f , is associated with a drier domain-mean and an increase in
 558 low-cloudiness in subsidence regions, LCF_d . The connection between clustering for a given
 559 A_f persists for LCF_d , but changes in the mean area of precipitation features and merid-
 560 ional and zonal shifts in heavy precipitation generally have weak relationships to the tropical-
 561 mean relative humidity, RH, independent of their relationship to A_f .

562 GCMs from the CMIP ensemble generally capture the observed tropical environ-
 563 ment signatures associated with changes in A_f , but often have different RH and LCF_d
 564 connections to shifts in heavy precipitation independent of A_f . In contrast to observa-

tions, RH in several models is sensitive to both meridional and zonal shifts in heavy precipitation. In CMIP6 models, zonal shifts of precipitation to the central Pacific tend to moisten, whereas meridional shifts to the equator tend to dry. Realistically represented or not, these sensitivities appear to affect how these models project relative humidity into the future; the subset of models sensitive to drying from meridional contraction of heavy precipitation create considerable spread in the model ensemble relative humidity changes under warming.

The study includes several limitations that are worth highlighting. Perhaps most importantly, the models we examined do not resolve the processes leading to organization of convection on mesoscales, which in turn may affect how they simulate heavy precipitation associated with large-scale convective features (Bao et al., 2017). This includes the high-resolution GCM, which still employs a parameterized convection scheme (Koldunov et al., 2023). Another limitation is that monthly anomalies from the climatology of the associated month obscure variations in diurnal and daily clustering tendencies and seasonal differences in the strength of relationships. Similarly, the climatological values do not control for variations in the contribution from different timescales, including diurnal up to seasonal and decadal variations in clustering. Finally, we note that our model ensemble is one of opportunity, and the models used were dictated by the available data. Correlation across the ensemble is not guaranteed to be produced by a physical relationship, and the extent to which such relationships arise by chance rise the more variables are examined. Nevertheless, the relationships between SST gradients and shifts in the precipitation distribution we highlight here are based on well-established physical relationships that provides some confidence in their robustness.

Future research is encouraged to adopt the control for total convective area, or other similar controls for changes in the mean precipitation rate, as used in the present framework. One avenue for further investigation is to identify models with realistic clustering compared to observations. The CMIP6 models considered here show a wide range in climatological clustering and internal variability in clustering, and perhaps a subset of models with more realistic clustering characteristics should be given more weight in projections of climate. In a similar way, investigating the connection between large-scale clustering and mesoscale clustering in high-resolution observations and storm resolving models may further constrain the model spread in projections by identifying unrealistic behavior. Further developing these research endeavors would allow for increased confidence and reduce the model uncertainty in aspects of projections that could be influenced by changes in convective organization, ultimately allowing for improvement in mitigation and adaptation strategies for a warming climate.

601 Open Research Section

602 CMIP models used in this study are listed in Table S1 and model output is avail-
603 able through the Earth System Grid Federation (ESGF) at <https://esgf-node.llnl.gov/search/cmip6/>.
604 Observational datasets and access are listed here; GPCP precipitation dataset: <https://doi.org/10.5065/ZGJD-9B02>, ERA5 dataset: <https://doi.org/10.24381/cds.adbb2d47>, NOAA surface temper-
605 ature dataset: <https://psl.noaa.gov/data/gridded/>, CERES outgoing longwave radia-
606 tion dataset: <https://ceres.larc.nasa.gov/data/>, ISCCP: ISCCP cloud states dataset: <https://isccp.giss.nasa.gov/a>
607 The IFS_9_FESOM_5 model data is available via the World Data Center for Climate (WDCC)
608 at DKRZ: https://doi.org/10.26050/WDCC/nextGEMS_cyc2. Code examples for repro-
609 ducing key metric calculations and figures are available at Blackberg (2025a). Key met-
610 rics are available at Blackberg (2025b).
611

Acknowledgments

We acknowledge the World Climate Research Programme's Working Group on Coupled Modelling, which is responsible for CMIP, and we thank the climate modeling groups (listed in Table S1 in the supporting information) for producing and making available their model output. Further, we acknowledge the Deutsches Klimarechenzentrum (DKRZ) for providing resources for using the Levante supercomputer, which facilitated the analysis of the nextGEMS Cycle 2 simulation: IFS_9_FESOM_5 used in this study. We also extend a special thank you to Dr. Cathy Hohenegger at Max Planck Institute for Meteorology for hosting the first author during a research visit to Hamburg, for providing guidance on model selection, and for facilitating access to institutional resources that greatly supported the analysis of the high-resolution GCM used in this study. Finally, we acknowledge support from the Australian Research Council (ARC) (grant no. DP230102077), the ARC Centre of Excellence for the Weather of the 21st Century (grant no. CE170100023), and computational resources and services from the National Computational Infrastructure, all funded by the Australian Government.

627 References

- Alexander, M. A., Bladé, I., Newman, M., Lanzante, J. R., Lau, N.-C., & Scott, J. D. (2002). The atmospheric bridge: The influence of enso teleconnections on air-sea interaction over the global oceans. *Journal of Climate*, 15(16), 2205 - 2231. Retrieved from https://journals.ametsoc.org/view/journals/clim/15/16/1520-0442.2002.015.2205.tabtio_2.0.co_2.xml doi: 10.1175/1520-0442(2002)015<2205:TABTIO>2.0.CO;2
- Arnold, N. P., & Randall, D. A. (2015). Global-scale convective aggregation: Implications for the madden-julian oscillation. *Journal of Advances in Modeling Earth Systems*, 7(4), 1499-1518. Retrieved from <https://agupubs.onlinelibrary.wiley.com/doi/abs/10.1002/2015MS000498> doi: <https://doi.org/10.1002/2015MS000498>
- Bao, J., Sherwood, S. C., Colin, M., & Dixit, V. (2017, 10). The robust relationship between extreme precipitation and convective organization in idealized numerical modeling simulations. *Journal of Advances in Modeling Earth Systems*, 9, 2291-2303. Retrieved from <https://agupubs.onlinelibrary.wiley.com/doi/full/10.1002/2017MS001125> doi: 10.1002/2017MS001125
- Blackberg, P. (2025a). *Large-scale clustering of tropical precipitation: Code repository*. Zenodo. Retrieved from <https://doi.org/10.5281/zenodo.17070290> ([Software]) doi: 10.5281/zenodo.17070290
- Blackberg, P. (2025b). *Metrics for large-scale clustering of tropical precipitation*. Zenodo. Retrieved from <https://doi.org/10.5281/zenodo.16946243> ([Dataset]) doi: 10.5281/zenodo.16946243
- Bläckberg, C. P., & Singh, M. S. (2022, 5). Increased large-scale convective aggregation in cmip5 projections: Implications for tropical precipitation extremes. *Geophysical Research Letters*, 49. Retrieved from <https://agupubs.onlinelibrary.wiley.com/doi/full/10.1029/2021GL097295> doi: 10.1029/2021GL097295
- Bony, S., Semie, A., Kramer, R. J., Soden, B., Tompkins, A. M., & Emanuel, K. A. (2020). Observed modulation of the tropical radiation budget by deep convective organization and lower-tropospheric stability. *AGU Advances*, 1(3), e2019AV000155. Retrieved from <https://agupubs.onlinelibrary.wiley.com/doi/abs/10.1029/2019AV000155> (e2019AV000155 10.1029/2019AV000155) doi: <https://doi.org/10.1029/2019AV000155>
- Bretherton, C. S., Blossey, P. N., & Khairoutdinov, M. (2005, December). An energy-balance analysis of deep convective self-aggregation above uniform sst. *Journal of the Atmospheric Sciences*, 62(12), 4273-4292. Retrieved from <http://dx.doi.org/10.1175/JAS3614.1> doi: 10.1175/jas3614.1
- Byrne, M. P., & Schneider, T. (2016). Energetic constraints on the width of the intertropical convergence zone. *Journal of Climate*, 29(13), 4709 - 4721. Retrieved from <https://journals.ametsoc.org/view/journals/clim/29/13/jcli-d-15-0767.1.xml> doi: 10.1175/JCLI-D-15-0767.1
- Emanuel, K., Wing, A. A., & Vincent, E. M. (2014, 2). Radiative-convective instability. *Journal of Advances in Modeling Earth Systems*, 6(1), 75–90. Retrieved from <http://dx.doi.org/10.1002/2013ms000270> doi: 10.1002/2013ms000270
- Eyring, V., Bony, S., Meehl, G. A., Senior, C. A., Stevens, B., Stouffer, R. J., & Taylor, K. E. (2016). Overview of the coupled model intercomparison project phase 6 (cmip6) experimental design and organization. *Geoscientific Model Development*, 9(5), 1937-1958. Retrieved from <https://gmd.copernicus.org/articles/9/1937/2016/> doi: 10.5194/gmd-9-1937-2016
- Hartmann, D. L., Hendon, H. H., & Houze, R. A. (1984). Some implications of the mesoscale circulations in tropical cloud clusters for large-scale dynamics and climate. *Journal of Atmospheric Sciences*, 41, 113 - 121. Retrieved from https://journals.ametsoc.org/view/journals/atsc/41/1/1520-0469_1984_041_0113_siotmc_2.0_co_2.xml doi: 10.1175/1520-0469(1984)041<0113:

- 681 SIOTMC>2.0.CO;2
- 682 Hausfather, Z., Marvel, K., Schmidt, G. A., Nielsen-Gammon, J. W., & Zelinka, M.
683 (2022). Climate simulations: Recognize the ‘hot model’ problem. *Nature*, *605*,
684 26–29. doi: 10.1038/d41586-022-01192-2
- 685 Hersbach, H., Bell, B., Berrisford, P., Horányi, A., Muñoz-Sabater, J., Nicolas, J., ...
686 Thépaut, J.-N. (2023). *Era5 hourly data on pressure levels from 1940 to present*.
687 Copernicus Climate Change Service (C3S) Climate Data Store. Retrieved from
688 <https://cds.climate.copernicus.eu/datasets/reanalysis-era5-pressure-levels> (Accessed: 2025-05-07) doi: 10.24381/cds.bd0915c6
- 689 Holloway, C. E., Wing, A. A., Bony, S., Muller, C., Masunaga, H., L'Ecuyer, T. S.,
690 ... Zuidema, P. (2017, November). Observing convective aggregation. *Surveys
691 in Geophysics*, *38*(6), 1199–1236. Retrieved from <https://link.springer.com/article/10.1007/s10712-017-9419-1> doi: 10.1007/s10712-017-9419-1
- 692 Huang, B., Yin, X., Menne, M. J., Vose, R. S., & Zhang, H.-M. (2024). *Noaa global
693 surface temperature dataset (noaglobaltemp), version 6.0.* NOAA National Cen-
694 ters for Environmental Information. Retrieved from <https://www.ncei.noaa.gov/access/metadata/landing-page/bin/iso?id=gov.noaa.ncdc%3AC01704>
695 doi: 10.25921/rzxg-p717
- 696 Huffman, G. J., Adler, R. F., Behrangi, A., Bolvin, D. T., Nelkin, E. J., Gu, G.,
697 & Ehsani, M. R. (2023). *The new version 3.2 global precipitation climatol-
698 ogy project (gpcp) monthly and daily precipitation products* (Vol. 36) (No. 21).
699 American Meteorological Society. Retrieved from <https://doi.org/10.1175/JCLI-D-23-0123.1> doi: 10.1175/JCLI-D-23-0123.1
- 700 Jones, P. W. (1999). First- and second-order conservative remapping schemes
701 for grids in spherical coordinates. *Monthly Weather Review*, *127*(9), 2204
702 - 2210. Retrieved from https://journals.ametsoc.org/view/journals/mwre/127/9/1520-0493_1999_127_2204_fasocr_2.0.co_2.xml doi: 10.1175/
703 1520-0493(1999)127<2204:FASOCR>2.0.CO;2
- 704 Koldunov, N., Kölling, T., Pedruzo-Bagazgoitia, X., Rackow, T., Redler, R.,
705 Sidorenko, D., ... Ziemen, F. A. (2023). *nextgems: output of the model de-
706 velopment cycle 3 simulations for icon and ifs.* World Data Center for Cli-
707 mate (WDCC) at DKRZ. Retrieved from https://doi.org/10.26050/WDCC/nextGEMS_cyc3 doi: 10.26050/WDCC/nextGEMS_cyc3
- 708 Maddox, R. A. (1980, November). Mesoscale convective complexes. *Bulletin of
709 the American Meteorological Society*, *61*(11), 1374–1387. Retrieved from [http://dx.doi.org/10.1175/1520-0477\(1980\)061<1374:MCC>2.0.CO;2](http://dx.doi.org/10.1175/1520-0477(1980)061<1374:MCC>2.0.CO;2) doi: 10.1175/
710 1520-0477(1980)061<1374:mcc>2.0.co;2
- 711 Mapes, B. E. (1993, July). Gregarious tropical convection. *Journal of the At-
712 mospheric Sciences*, *50*(13), 2026–2037. Retrieved from [http://dx.doi.org/10.1175/1520-0469\(1993\)050<2026:gtc>2.0.co;2](http://dx.doi.org/10.1175/1520-0469(1993)050<2026:GTC>2.0.CO;2) doi: 10.1175/
713 1520-0469(1993)050<2026:gtc>2.0.co;2
- 714 Mapes, B. E., & Houze, R. A. (1993, May). Cloud clusters and superclusters
715 over the oceanic warm pool. *Monthly Weather Review*, *121*(5), 1398–1416.
716 Retrieved from [http://dx.doi.org/10.1175/1520-0493\(1993\)121<1398:ccasot>2.0.co;2](http://dx.doi.org/10.1175/1520-0493(1993)121<1398:CCASOT>2.0.CO;2) doi: 10.1175/
717 1520-0493(1993)121<1398:ccasot>2.0.co;2
- 718 Mardia, K. V., Kent, J. T., & Bibby, J. M. (1979). *Multivariate analysis*. London:
719 Academic Press.
- 720 NOAA Physical Sciences Laboratory, Climate Prediction Center. (2025). *Cpc
721 daily blended outgoing longwave radiation (olr) – 1° × 1°.* <https://psl.noaa.gov/data/gridded/data.cpc.blended.olr-1deg.html>. (Daily OLR data
722 (1991–present); please acknowledge NOAA PSL when using)
- 723 Pendergrass, A. G., Reed, K. A., & Medeiros, B. (2016). The link between extreme
724 precipitation and convective organization in a warming climate: Global radiative-
725 convective equilibrium simulations. *Geophysical Research Letters*, *43*(21), 11,445-

- 735 11,452. Retrieved from <https://agupubs.onlinelibrary.wiley.com/doi/abs/10.1002/2016GL071285> doi: <https://doi.org/10.1002/2016GL071285>
- 736 Popp, M., & Bony, S. (2019). Stronger zonal convective clustering associated with a
737 wider tropical rain belt. *Nature Communications*, 10, 4261. doi: 10.1038/s41467-019-12167-9
- 740 Quan, H., Zhang, B., Wang, C., & Fueglistaler, S. (2025). The sea surface tem-
741 perature pattern effect on outgoing longwave radiation: The role of large-scale
742 convective aggregation. *Geophysical Research Letters*, 52(11), e2024GL112756.
743 Retrieved from <https://agupubs.onlinelibrary.wiley.com/doi/abs/10.1029/2024GL112756> (e2024GL112756) doi: <https://doi.org/10.1029/2024GL112756>
- 746 Retsch, M. H., Jakob, C., & Singh, M. S. (2020, 4). Assessing convective organiza-
747 tion in tropical radar observations. *Journal of Geophysical Research: Atmospheres*,
748 125. doi: 10.1029/2019JD031801
- 749 Schiro, K., Su, H., Ahmed, F., Dai, N., Singer, C., Gentine, P., ... Neelin, J.
750 (2022, 11). Model spread in tropical low cloud feedback tied to overturning
751 circulation response to warming. *Nature Communications*, 13, 7119. Retrieved
752 from <https://www.nature.com/articles/s41467-022-34787-4> doi:
753 10.1038/s41467-022-34787-4
- 754 Semie, A. G., & Bony, S. (2020). Relationship between precipitation extremes
755 and convective organization inferred from satellite observations. *Geophysical
756 Research Letters*, 47(9), e2019GL086927. Retrieved from <https://agupubs.onlinelibrary.wiley.com/doi/abs/10.1029/2019GL086927> (e2019GL086927)
757 10.1029/2019GL086927 doi: <https://doi.org/10.1029/2019GL086927>
- 759 Sobel, A. H., Held, I. M., & Bretherton, C. S. (2002). The enso signal in tropical
760 tropospheric temperature. *Journal of Climate*, 15(18), 2702 - 2706. Retrieved
761 from https://journals.ametsoc.org/view/journals/clim/15/18/1520-0442_2002_015_2702_tesitt_2.0.co_2.xml doi: 10.1175/1520-0442(2002)015<2702:TESITT>2.0.CO;2
- 764 Tobin, I., Bony, S., Holloway, C. E., Grandpeix, J.-Y., Sèze, G., Coppin, D., ...
765 Roca, R. (2013). Does convective aggregation need to be represented in cumulus
766 parameterizations? *Journal of Advances in Modeling Earth Systems*, 5(4), 692-
767 703. Retrieved from <https://agupubs.onlinelibrary.wiley.com/doi/abs/10.1002/jame.20047> doi: <https://doi.org/10.1002/jame.20047>
- 769 Tselioudis, G., Tromeur, E., Rossow, W. B., & Zerefos, C. S. (2010, 7). Decadal
770 changes in tropical convection suggest effects on stratospheric water vapor. *Geo-
771 physical Research Letters*, 37. doi: 10.1029/2010GL044092
- 772 Watanabe, M., Kang, S. M., Collins, M., Hwang, Y.-T., McGregor, S., & Stuecker,
773 M. F. (2024). Possible shift in controls of the tropical pacific surface warming
774 pattern. *Nature*, 630(8016), 315-324. Retrieved from <https://www.nature.com/articles/s41586-024-07452-7> doi: 10.1038/s41586-024-07452-7
- 776 Wheeler, M., & Kiladis, G. N. (1999). Convectively coupled equatorial waves: Anal-
777 ysis of clouds and temperature in the wavenumber-frequency domain. *Journal
778 of the Atmospheric Sciences*, 56, 374-399. Retrieved from https://journals.ametsoc.org/view/journals/atsc/56/3/1520-0469_1999_056_0374_ccewao_2.0.co_2.xml doi: 10.1175/1520-0469(1999)056<0374:CCEWAO>2.0.CO;2
- 781 Williams, A. I. L., Jeevanjee, N., & Bloch-Johnson, J. (2023). Circus tents, con-
782 vective thresholds, and the non-linear climate response to tropical ssts. *Geophys-
783 ical Research Letters*, 50(6), e2022GL101499. Retrieved from <https://agupubs.onlinelibrary.wiley.com/doi/abs/10.1029/2022GL101499> (e2022GL101499)
784 2022GL101499 doi: <https://doi.org/10.1029/2022GL101499>
- 786 Wills, R. C. J., Dong, Y., Proistosecu, C., Armour, K. C., & Battisti, D. S. (2022,
787 September). Systematic climate model biases in the large-scale patterns of recent
788 sea-surface temperature and sea-level pressure change. *Geophysical Research Let-*

- ters, 49(17). Retrieved from <http://dx.doi.org/10.1029/2022GL100011> doi: 10.1029/2022gl100011
- Wing, A. A., Emanuel, K., Holloway, C. E., & Muller, C. (2018). Convective self-aggregation in numerical simulations: A review. In R. Pincus, D. Winker, S. Bony, & B. Stevens (Eds.), *Shallow clouds, water vapor, circulation, and climate sensitivity* (pp. 1–25). Cham: Springer International Publishing. Retrieved from https://doi.org/10.1007/978-3-319-77273-8_1 doi: 10.1007/978-3-319-77273-8_1
- Wing, A. A., & Emanuel, K. A. (2014). Physical mechanisms controlling self-aggregation of convection in idealized numerical modeling simulations. *Journal of Advances in Modeling Earth Systems*, 6(1), 59–74. Retrieved from <https://agupubs.onlinelibrary.wiley.com/doi/abs/10.1002/2013MS000269> doi: <https://doi.org/10.1002/2013MS000269>
- Wodzicki, K. R., & Rapp, A. D. (2016). Long-term characterization of the pacific itcz using trmm, gpcp, and era-interim. *Journal of Geophysical Research: Atmospheres*, 121(7), 3153–3170. Retrieved from <https://agupubs.onlinelibrary.wiley.com/doi/abs/10.1002/2015JD024458> doi: <https://doi.org/10.1002/2015JD024458>
- Young, A. H., Knapp, K. R., Inamdar, A., Hankins, W., & Rossow, W. B. (2018). The international satellite cloud climatology project h-series climate data record product. *Earth System Science Data*, 10(1), 583–593. Retrieved from <https://essd.copernicus.org/articles/10/583/2018/> doi: 10.5194/essd-10-583-2018
- Zelinka, M. D., Myers, T. A., McCoy, D. T., Po-Chedley, S., Caldwell, P. M., Ceppli, P., ... Taylor, K. E. (2020). Causes of higher climate sensitivity in cmip6 models. *Geophysical Research Letters*, 47(1), e2019GL085782. Retrieved from <https://agupubs.onlinelibrary.wiley.com/doi/full/10.1029/2019GL085782>